




What Drives Chorismate Mutase to Top Performance? Insights from a Combined In Silico and In Vitro Study

Journal Article

Author(s):

Thorbjørnsrud, Helen V.; Bressan, Luca; Khatanbaatar, Tamjidmaa; Carrer, Manuel; [Würth-Roderer, Kathrin](#) ; Cordara, Gabriele; [Kast, Peter](#) ; Cascella, Michele; [Krengel, Ute](#) 

Publication date:

2023-02-07

Permanent link:

<https://doi.org/10.3929/ethz-b-000599925>

Rights / license:

[Creative Commons Attribution 4.0 International](#)

Originally published in:

Biochemistry 62(3), <https://doi.org/10.1021/acs.biochem.2c00635>

Funding acknowledgement:

182648 - Exploring structure, function, and mechanism of atypical bacterial chorismate mutases (SNF)

What Drives Chorismate Mutase to Top Performance? Insights from a Combined *In Silico* and *In Vitro* Study

Helen V. Thorbjørnsrud,^{||} Luca Bressan,^{||} Tamjidmaa Khatanbaatar,^{||} Manuel Carrer, Kathrin Würth-Roderer, Gabriele Cordara, Peter Kast,^{*} Michele Cascella,^{*} and Ute Krenkel^{*}



Cite This: *Biochemistry* 2023, 62, 782–796



Read Online

ACCESS |



Metrics & More

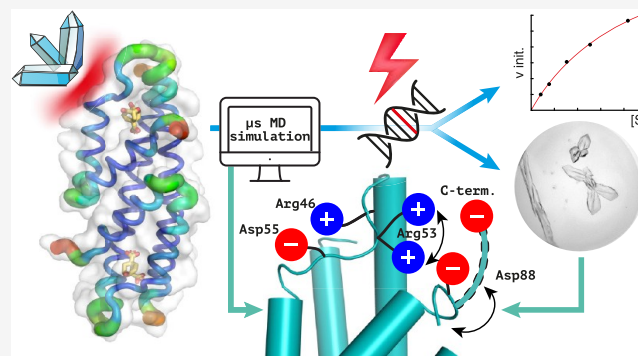


Article Recommendations



Supporting Information

ABSTRACT: Unlike typical chorismate mutases, the enzyme from *Mycobacterium tuberculosis* (MtCM) has only low activity on its own. Remarkably, its catalytic efficiency $k_{\text{cat}}/K_{\text{m}}$ can be boosted more than 100-fold by complex formation with a partner enzyme. Recently, an autonomously fully active MtCM variant was generated using directed evolution, and its structure was solved by X-ray crystallography. However, key residues were involved in crystal contacts, challenging the functional interpretation of the structural changes. Here, we address these challenges by microsecond molecular dynamics simulations, followed up by additional kinetic and structural analyses of selected sets of specifically engineered enzyme variants. A comparison of wild-type MtCM with naturally and artificially activated MtCMs revealed the overall dynamic profiles of these enzymes as well as key interactions between the C-terminus and the active site loop. In the artificially evolved variant of this model enzyme, this loop is preorganized and stabilized by Pro52 and Asp55, two highly conserved residues in typical, highly active chorismate mutases. Asp55 stretches across the active site and helps to appropriately position active site residues Arg18 and Arg46 for catalysis. The role of Asp55 can be taken over by another acidic residue, if introduced at position 88 close to the C-terminus of MtCM, as suggested by molecular dynamics simulations and confirmed by kinetic investigations of engineered variants.

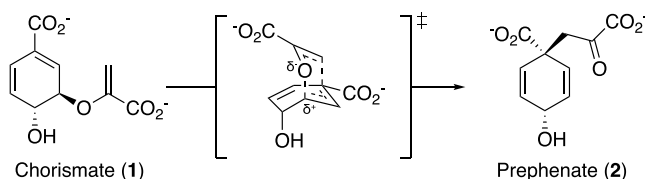


INTRODUCTION

Pericyclic reactions are common in industrial processes, but very rare in biology.^{1–4} Chorismate mutase (CM) catalyzes the only known pericyclic process in primary metabolism, the Claisen rearrangement of chorismate (1) to prephenate (2), *via* a chair-like transition state (Scheme 1).⁵ This catalytic step at the branch point of the shikimate pathway funnels the key metabolite chorismate toward the synthesis of tyrosine and phenylalanine, as opposed to tryptophan and several aromatic vitamins.^{6,7} The CM reaction is a concerted unimolecular transformation that is well studied by both experimental and computational means.⁸ It proceeds ostensibly *via* the same transition state in both solution and enzyme catalysis.^{9,10} Due to these factors, CM has long been a model enzyme for computational chemists.¹¹

Natural CMs belong to two main classes with two distinct folds AroH and AroQ, which are equally efficient, with typical $k_{\text{cat}}/K_{\text{m}}$ values in the range of $(1–5) \times 10^5 \text{ M}^{-1} \text{ s}^{-1}$.¹² The AroH fold, exemplified by the *Bacillus subtilis* CM, has a trimeric pseudo- α/β -barrel structure,^{13,14} whereas the structures of AroQ enzymes have all- α -helical folds.^{15–21} The AroQ family is further divided into four subfamilies, α – δ .^{20,21} The AroQ _{δ} subfamily shows abnormally low catalytic activity

Scheme 1. Chorismate Mutase Reaction⁴



⁴The Claisen rearrangement catalyzed by chorismate mutase converts chorismate (1) to prephenate (2) and proceeds *via* a highly polarized chair-like transition state carrying partial charges at the C–O bond that is broken during the reaction.

compared to prototypical CM enzymes. In fact, the first discovered AroQ _{δ} enzyme, the intracellular CM from *Mycobacterium tuberculosis* (MtCM),^{20,21} is on its own only a

Received: November 8, 2022

Revised: December 18, 2022

Published: January 27, 2023



poor catalyst ($k_{\text{cat}}/K_m = 1.8 \times 10^3 \text{ M}^{-1} \text{ s}^{-1}$),²¹ despite its crucial role for producing the aromatic amino acids Tyr and Phe. However, this low activity can be boosted more than 100-fold to a k_{cat}/K_m of $2.4 \times 10^5 \text{ M}^{-1} \text{ s}^{-1}$ through formation of a noncovalent complex with the first enzyme of the shikimate pathway, 3-deoxy-D-arabino-heptulosonate 7-phosphate (DAHPP) synthase (MtDS) (Figure 1A).²¹

The active site of AroQ CMs is dominated by positive charges, contributed by four arginine residues (Figure 1F). In MtCM, these are Arg18', Arg35, Arg46, and Arg58 (with the prime denoting a different MtCM protomer). Of particular importance for catalysis is Arg46,²¹ or its corresponding cationic residues in other CMs (of both AroH and AroQ families).²² However, high catalytic prowess is only achieved when this cationic residue is optimally positioned such that it can stabilize the developing negative charge at the ether oxygen in the transition state (Scheme 1).^{11,14,21,23–25} In MtCM, this is not the case unless MtCM is activated by MtDS.²¹ The MtDS partner repositions residues of the C-terminus of MtCM for interaction with the H1–H2 loop of MtCM that covers its active site, thereby inducing a characteristic kink in this loop (orange circle in Figure 1C). This interaction leads to a rearrangement of active site residues to catalytically more favorable conformations (Figure 1B)²¹ and is likely a key contributing factor for the increase in CM activity, as shown by randomizing mutagenesis of the C-terminal region followed by selection for functional variants.²⁶ Complex formation also endows MtCM with feedback regulation by Tyr and Phe through binding of these effectors to the MtDS partner.^{21,27,28} Such inter-enzyme allosteric regulation²⁸ allows for dynamic adjustment of the CM activity to meet the changing needs of the cell.

The naturally low activity of MtCM in the absence of its MtDS partner enzyme also provided a unique opportunity for laboratory evolution studies aimed at increasing MtCM efficiency. After four major rounds of directed evolution, the top-performing MtCM variant N-s4.15 emerged,¹² which is abbreviated as MtCM^V in this manuscript. This variant showed autonomous CM activity ($k_{\text{cat}}/K_m = 4.7 \times 10^5 \text{ M}^{-1} \text{ s}^{-1}$) twice exceeding that of wild-type MtCM in the MtCM–MtDS complex, and can no longer be activated further through the addition of MtDS.¹² The biggest gains in catalytic activity were due to replacements T52P and V55D in the H1–H2 loop and R87P, L88D, G89A, and H90M at the C-terminus (Figure 1C–E). Of these residues, Pro52 and Asp55 are conserved in the H1–H2 loop of naturally highly active CMs, such as the prototypic CMs from the α - and γ -AroQ subclasses, *i.e.*, EcCM from *Escherichia coli*¹⁶ and *MtCM, the secreted CM from *M. tuberculosis*,²⁰ respectively.¹² The single amino acid exchange that had the largest beneficial effect on activity was V55D (12-fold enhancement of k_{cat}/K_m), followed by T52P (6-fold gain).¹² Combined, these two changes, discussed in detail in a previous publication, gave a k_{cat}/K_m that was 22 times higher compared to wild-type MtCM.¹² The four C-terminal amino acid replacements together increased the activity more modestly (by a factor of 4), and the five exchanges introduced in the two final evolutionary rounds yielded an additional factor of 5. The resulting combination of large-impact and more subtle residue substitutions in MtCM^V (Figure 1D,E) gave a k_{cat}/K_m about 500 times greater than that of the parental starting point, thereby reaching the values of the most efficient CMs known to date.¹²

The crystal structure of MtCM^V revealed a strongly kinked conformation of the H1–H2 loop. This is reminiscent of the conformation adopted by MtCM when in the complex with MtDS (the crystal structure of MtDS-bound MtCM is in the following referred to as MtCM^{DS}) and differs considerably from that observed in free MtCM (Figure 1C,D).¹² However, in the crystal structures of free wild-type and top-evolved MtCM^V, both the H1–H2 loop and the C-terminus are involved in extensive crystal contacts, making an unbiased structural evaluation of the sequence alterations in these parts of the enzyme impossible. In solution, these regions are assumed to be more flexible compared to the α -helical segments of MtCM.

Here, we used molecular dynamics (MD) simulations to investigate the behavior of MtCM in the absence or presence of ligands and to analyze whether the protein is able to interconvert between activated and nonactivated conformations in the absence of the MtDS partner enzyme. We also compared the wild-type MtCM with the evolved MtCM^V, to see if the acquired amino acid substitutions introduced any new interactions or if they altered the probabilities of existing ones, with potential impact on catalytic activity. From an assessment of the dynamic properties of MtCM and MtCM^V, we proposed a set of single, double, and triple C-terminal variants of the enzyme and subsequently tested these experimentally.

MATERIALS AND METHODS

Construction of Untagged MtCM Variants. General cloning was carried out in *E. coli* DH5 α or XL1-Blue (both Stratagene, La Jolla, California). All cloning techniques and bacterial culturing were performed according to standard procedures.²⁹ Oligonucleotide synthesis and DNA sequencing were performed by Microsynth AG (Balgach, Switzerland).

For the construction of expression plasmids pKTCMM-H-V55D and pKTCMM-H-T52P for the native MtCM single variants, the individual site-directed mutants were first constructed in the pKTNTET background (providing an N-terminal His₆ tag, first 5 residues missing). Parts of the MtCM gene (Gene Rv0948c) were amplified using oligonucleotides 412-MtCM-N-V55D (5'-GTTCGCTAGCGGAGGTA-CACGTTTGGATCATAGTCGGGAGATGAAGGTCATC-GAAC) or 413-MtCM-N-T52P (5'-GTTCGCTAGCG-GAGGTCGCGTTTGGTCCATAGTCGGGAGAT-GAAGGTCATCGAAC) together with oligonucleotides 386-LpLib-N2 (5'-GGTTAAAGCTTCCGCAGCCACTAGT-TATTAGTGACCGAGGCGGCCACGGCCCAAT) on template pMG248¹² to create a 163 bp PCR product. The PCR products were restriction digested with *Nhe*I and *Hind*III and the resulting 148 bp fragments were individually ligated to the accordingly cut 2873 bp fragment from acceptor vector pKTNTET-0.¹² The ligation was performed with T4 DNA ligase (New England Biolabs, Ipswich, Massachusetts) overnight at 16 °C. The ligation products were transformed into chemically competent *E. coli* XL1-Blue cells. The cloned PCR'd DNA fragments were confirmed by Sanger sequencing. Subsequently, the genes for MtCM-T52P and MtCM-V55D were isolated by restriction digestion using enzymes *Xho*I and *Spe*I followed by a preparative agarose gel, yielding corresponding 260 bp fragments. pKTCMM-H²¹ was used as acceptor vector and was accordingly restriction digested with *Xho*I and *Spe*I, yielding a 4547 bp acceptor fragment. The fragments were ligated overnight at 16 °C, using T4 DNA

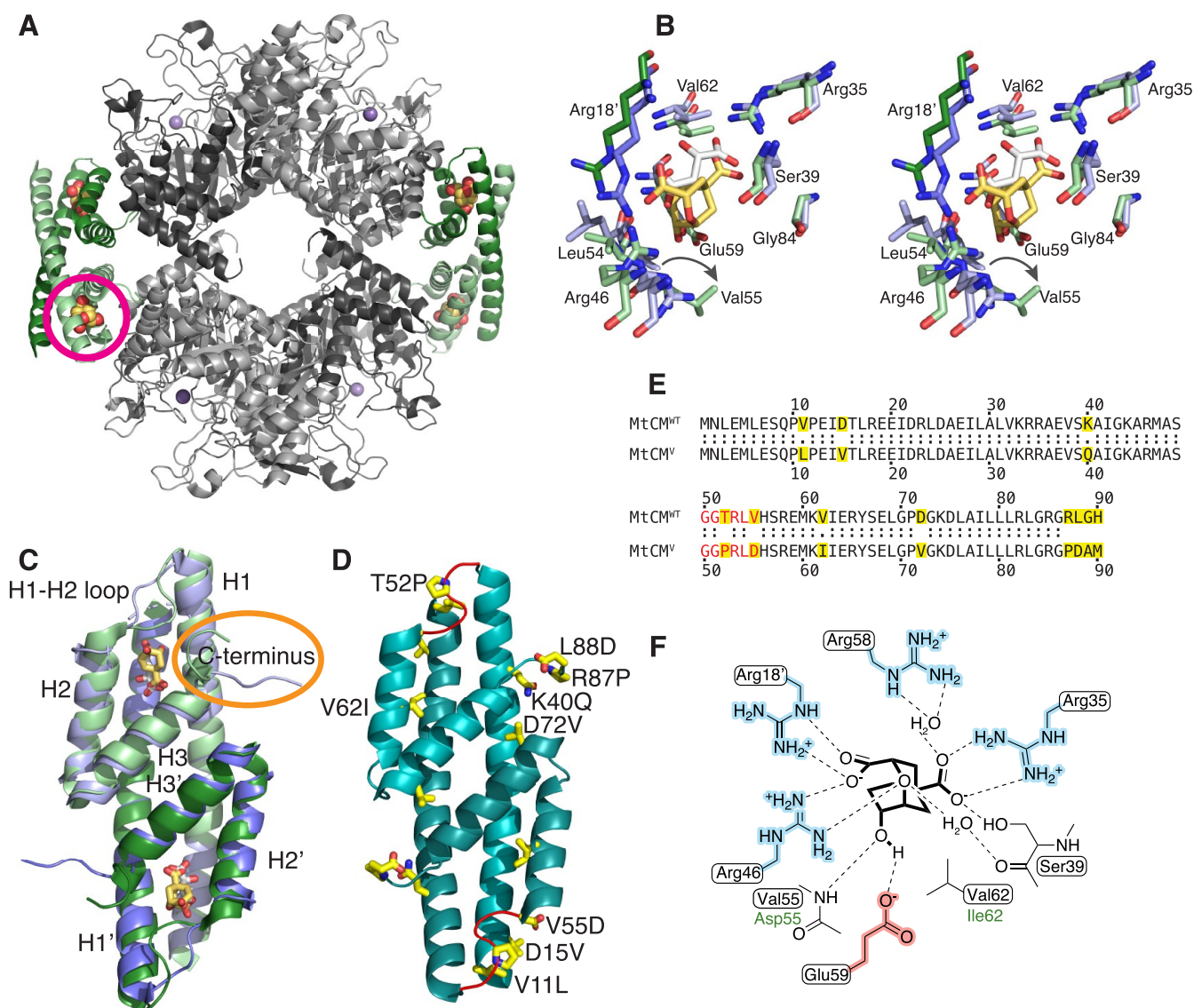


Figure 1. Structural information on *M. tuberculosis* chorismate mutase. (A) Cartoon illustration of the heterooctameric complex of MtCM with DAHP synthase (MtDS) (Protein Data Bank (PDB) ID: 2W1A).²¹ MtCM is colored in shades of green and MtDS in shades of gray to emphasize individual subunits; Bartlett's transition state analogue (TSA)⁵¹ is shown with golden spheres. The location of one of the four active sites of MtCM is marked with a circle. (B) Stereo superimposition of CM active sites of MtCM (shades of violet, with malate bound, white sticks) (PDB ID: 2VKL)²¹ and of the MtCM–MtDS complex (with TSA bound, golden sticks) (PDB ID: 2W1A),²¹ showing several active site residues as sticks. Shades of violet/green (and prime notation for Arg18') illustrate separate protomers of MtCM/MtCM–MtDS structures, respectively. An arrow shows the shift in the position of Val55 upon MtDS binding, allowing H-bond formation of its backbone to TSA. (C) Cartoon superimposition of MtCM (PDB ID: 2VKL;²¹ violet, with white sticks for malate ligand) and activated MtCM (MtCM^{DS}) from the MtCM–MtDS complex (PDB ID: 2W1A;²¹ green, with golden sticks for TSA). The biggest structural changes upon activation are a kink observed in the H1–H2 loop and interaction of the C-terminus (circled in orange) with the active site of MtCM. (D) Cartoon representation of the artificially evolved MtDS-independent super-active MtCM variant N-s4.15 (PDB ID: SMPV;¹² cyan), dubbed MtCM^V in this work, having a k_{cat}/K_m typical for the most efficient CMs known to date.¹² Amino acid replacements accumulated after four cycles of directed evolution are emphasized as yellow side-chain sticks (A89 and M90 are not resolved) and labeled for one of the protomers. The H1–H2 loop (shown in red) adopts a kinked conformation similar to that observed for the MtDS-activated MtCM^{DS} shown in (C). (E) Sequence alignment of wild-type MtCM (MtCM^{WT}) and the highly active variant N-s4.15 (MtCM^V).¹² Substituted residues are highlighted in yellow, and the H1–H2 loop is colored red. (F) Schematic representation of the active site of MtCM with bound TSA. Boxed residues refer to the wild-type enzyme, and green font color (Asp55, Ile62) refers to those substituted in MtCM^V. Charged residues are highlighted in red and blue.

ligase. The ligation products were transformed into chemically competent *E. coli* KA12 cells²³ and the inserts were analyzed by Sanger sequencing. The gene for variant PHS10-3p3,¹² carrying an N-terminal His₆-tag and missing the first five residues, was recloned into the native format provided by plasmid pKTCMM-H. Acceptor vector pKTCMM-H and

pKTNTET-PHS10-3p3 were restriction digested with *Xho*I and *Spe*I, and the fragments were isolated from preparative agarose gels. The 4547 bp and 260 bp fragments were ligated overnight at 16 °C with T4 DNA ligase and transformed into chemically competent XL1-Blue cells. The relevant gene sequence was confirmed by Sanger sequencing.

Different C-terminal variants of the MtCM gene were generated by PCR mutagenesis. DNA fragments were amplified with the same forward primer (containing an *NdeI* site, underlined) and different reverse primers (containing an *SpeI* site, underlined) on different DNA templates. The gene encoding MtCM L88D was produced by PCR with primers LB5 (5'-TCCGCACATATGAACCTGGAAATG) and LB4 (5'-TAAGCAACTAGTTATTAGTGACCGTCGCG) on the template plasmid pKTCMM-H carrying the wild-type gene.²¹ The gene for the triple variant MtCM (T52P V55D L88D) was assembled with primers LB5 and LB4 on a pKTCMM-H derivative containing MtCM variant 3p3 (T52P V55D).¹² The gene for MtCM variant PNAME (D88N) was generated with primers LB5 and LB6 (5'-TAAGCAACTAGTTATTACATAGCATTTCGGA), and for the MtCM variant PLAM (D88L) with primers LB5 and LB7 (5'-TAAGCAACTAGTTATTAGTGACCAAGCGGA), in both cases using a version of the template plasmid pKTCMM-H, into which the gene for the top-evolved s4.15 variant had been inserted.¹² The resulting 296 bp PCR fragments containing *NdeI* and *SpeI* restriction sites at the 5' and 3' ends of the MtCM gene, respectively, were digested with the corresponding enzymes to yield 278 bp fragments. These fragments were ligated to the 4529 bp *NdeI*–*SpeI* fragment of pKTCMM-H yielding the final 4807 bp plasmids.

Protein Production and Purification. *E. coli* strain KA13^{18,30} carrying an endogenous UV5 P_{lac} -expressed T7 RNA polymerase gene was used to overproduce the (untagged) MtCM variants. KA13 cells were transformed by electroporation with the appropriate pKTCMM-H plasmid derivative that carries the desired MtCM gene variant.

For the two crystallized MtCM variants T52P (MtCM^{T52P}) and V55D (MtCM^{V55D}), the transformed cells were grown in baffled flasks at 30 °C in LB medium containing 100 μ g/mL sodium ampicillin until the OD₆₀₀ reached 0.5. Gene expression was induced through the addition of isopropyl- β -D-thiogalactopyranoside (IPTG) to a final concentration of 0.5 mM, and incubation was continued overnight. The cells were harvested by centrifugation (6500g for 20 min at 4 °C) and frozen at –80 °C before being resuspended in a buffer suitable for ion exchange chromatography, supplemented with DNase I (Sigma), 150 μ M phenylmethanesulfonyl fluoride (PMSF) and cOmplete protease inhibitor cocktail (Roche). The cells were lysed using BeadBeater (BioSpec BSP 74340, Techtum Lab AB), with four times 30 s pulses with a 60 s wait between each pulse. Insoluble debris was removed by centrifugation (48,000g for 30 min at 4 °C).

The resuspension buffer was selected based on the theoretical isoelectric point (pI) of the protein. MtCM T52P has a pI of 8.14, so the pellet was resuspended in 50 mM 2-(*N*-morpholino)ethanesulfonic acid (MES), pH 6.5. MtCM V55D has a pI of 6.74; therefore, the pellet was resuspended in 50 mM acetic acid, pH 5.25. After lysis and centrifugation, the soluble lysate was loaded onto a HiTrap XL SP column (GE Healthcare) for cation exchange chromatography and eluted with a 0–0.5 M NaCl gradient. The purity of the eluted fractions was gauged by sodium dodecyl sulfate polyacrylamide gel electrophoresis (SDS-PAGE) analysis and sufficiently pure fractions were pooled and concentrated using concentrator tubes with a 5 kDa molecular mass cutoff (Vivaspin MWCO 5K). The proteins were then further purified by size-exclusion chromatography using a Superdex 75 300/10 column (GE Healthcare) with running buffer 20 mM 1,3-bis[tris-

(hydroxymethyl)methylamino]propane (BTP), pH 7.5, 150 mM NaCl. Finally, the proteins were concentrated (Vivaspin MWCO 5K), frozen, and stored at –80 °C.

For the sets of MtCM variants probed for the catalytic impact of particular C-terminal amino acid exchanges, 500 mL LB medium cultures containing 150 μ g mL^{–1} sodium ampicillin were inoculated with 5 mL overnight culture of the desired transformant and grown at 37 °C and 220 rpm shaking to an OD_{600nm} of 0.3–0.5. Protein production was induced by the addition of IPTG to 0.5 mM, and culture growth was continued overnight at 30 °C.

The cells were harvested by centrifugation (17,000g for 10 min at 4 °C) and washed once with 100 mM tris(hydroxymethyl)aminomethane (Tris)–HCl, pH 7.5. The cells were pelleted again, and the cell pellet was either frozen for storage at –20 °C or directly resuspended in 80 mL of sonication buffer (50 mM sodium phosphate, 0.3 M NaCl, pH 7.0). The cells were disrupted by sonication on ice (15 min total pulse time with 45 s pulse/30 s pause cycles at 50% amplitude; Q700 sonicator, QSonica). The crude lysate was cleared by centrifugation (20,000g for 20 min at 4 °C). The supernatant was supplemented with sonication buffer to 100 mL, 42 g of ammonium sulfate was added, and the solution was stirred at 4 °C for 1.5 h. The precipitate was pelleted by centrifugation (10,000g for 30 min at 4 °C), dissolved in 8 mL of low-salt buffer (20 mM piperazine, pH 9.0), and dialyzed against 1 L of low-salt buffer overnight. Dialysis was repeated against another 1 L of low-salt buffer for 3 h before application to a MonoQ (MonoQ HR 10/10, Pharmacia) FPLC column (Biologic Duoflow system, Bio-Rad). The sample was eluted over 80 mL in 20 mM piperazine by applying a gradient from 0 to 30% of a high-salt buffer (20 mM piperazine, 1 M NaCl, pH 9.0).

The MonoQ fractions containing the protein of interest were pooled and concentrated to less than 1 mL. The concentrated sample was directly applied to a gel-filtration column (Superdex Increase 75 10/300 GL, GE Healthcare) and eluted in 20 mM BTP, 150 mM NaCl, pH 7.5. Protein identity was confirmed by liquid chromatography–mass spectrometry (LC-MS) (MoBiAS facility, Laboratory of Organic Chemistry, ETH Zurich), with the observed mass being within 1 Da of the calculated mass. Protein purity was assessed by SDS-PAGE (PhastGel Homogenous 20 precast gels, GE Healthcare) and the enzyme concentration ($[E]$) was determined using the Bradford assay.³¹

X-ray Crystallography. MtCM variants T52P (MtCM^{T52P}) and V55D (MtCM^{V55D}) were crystallized in 96-well two-drop MRC crystallization plates (SWISSCI) by the sitting drop vapor diffusion technique. Diffraction-quality crystals of MtCM^{T52P} grew at 20 °C from a 1:1 (375 nL + 375 nL) mixture of protein (28 mg mL^{–1} in 20 mM BTP, pH 7.5) and reservoir solution containing 0.2 M sodium malonate, 20% PEG 3350 (w/v), and 0.1 M Bis Tris propane buffer, pH 8.5 (PACT premier crystallization screen, condition H12; Molecular Dimensions Ltd.). Crystals of MtCM^{V55D} were obtained from a 1:1 (375 nL + 375 nL) mixture of protein (44 mg mL^{–1} in 20 mM Bis Tris propane, pH 7.5, 150 mM NaCl) and reservoir solution containing 0.2 M zinc acetate dihydrate, 10% w/v PEG 3000, and 0.1 M sodium acetate, pH 4.5 (JCSG-plus crystallization screen, condition C7; Molecular Dimensions Ltd.) at 20 °C.

Diffraction data of MtCM^{T52P} and MtCM^{V55D} crystals were collected at the European Synchrotron Radiation Facility

(ESRF, Grenoble, France) at the ID30A-3/MASSIF-3 (Dectris Eiger X 4M detector) and ID29 (Pilatus detector) beamlines, respectively, covering 120° with 0.1° oscillation. Diffraction images were integrated and scaled using the XDS software package;³² merging and truncation were performed with AIMLESS³³ from the CCP4 program suite.³⁴ Since data collection statistics of both crystals suggested the presence of anisotropy, the XDS output was reprocessed for anisotropy correction and truncation using the STARANISO server.³⁵ The “aniso-merged” output files (merged MTZ file with an anisotropic diffraction cutoff) were subsequently used for structure solution and refinement (Table S1).

The crystal structures of MtCM^{T52P} and MtCM^{V55D} were solved by molecular replacement with the program Phaser.³⁶ The structure of the top-evolved MtCM variant MtCM^V (PDB ID: SMPV)¹² was used as a search model for solving the structure of MtCM^{T52P} since it was expected to be a better match at the Pro52-containing H1–H2 loop compared to wild-type MtCM. For MtCM^{V55D}, we used the MtCM structure from the MtCM–MtDS complex (PDB ID: 2W1A)²¹ as a search model, after truncation of the termini and the H1–H2 loop, and removal of the ligand.

The two structures were subsequently refined, alternating between real-space refinement cycles using Coot³⁷ and maximum-likelihood refinement with REFMAC5.³⁸ The models were improved stepwise by first removing ill-defined side chains, and subsequently adding missing structural elements as the quality of the electron density map improved. Water molecules and alternative side-chain conformations were added to the MtCM^{T52P} model toward the end of the refinement process, where positive peaks in the σ_A -weighted $F_o - F_c$ difference map and the chemical surroundings allowed for their unambiguous identification. As a last step, occupancy refinement was carried out with phenix.refine, a tool of the PHENIX software suite.³⁹ The final structure of MtCM^{T52P} was deposited in the Protein Data Bank (PDB)⁴⁰ with deposition code 6YGT. Data collection and refinement statistics are summarized in Supporting Table S1.

Determination of Enzyme Kinetic Parameters.

Michaelis–Menten kinetics of the untagged purified MtCM variants were determined by a continuous spectroscopic chorismate depletion assay (Lambda 20 UV/VIS spectrophotometer, PerkinElmer). The purified enzymes were diluted into 20 mM potassium phosphate, pH 7.5, containing 0.01 mg mL⁻¹ bovine serum albumin to obtain suitable working concentrations for starting the reactions, depending on the activity of individual variants. The assays were performed at 30 °C in either 50 mM potassium phosphate, pH 7.5, or 50 mM BTP, pH 7.5. Different chorismate concentrations ($[S]$) ranging from 10 to 1500 μ M were used at 274 nm ($\epsilon_{274} = 2630$ M⁻¹ cm⁻¹) or 310 nm ($\epsilon_{310} = 370$ M⁻¹ cm⁻¹). Chorismate disappearance upon enzyme addition was monitored to determine the initial reaction velocity (v_0). The obtained data were fitted to the Michaelis–Menten equation with the program KaleidaGraph (Synergy Software, Reading, Pennsylvania) to obtain the catalytic parameters k_{cat} and K_m .

Molecular Dynamics Simulations. Molecular dynamics (MD) simulations were carried out on a number of representative structures for CM. They included two independent sets of simulations for apo MtCM, starting either from the X-ray crystal structure of MtCM in complex with malate (after removing malate) (PDB ID: 2VKL)²¹ or from the structure of the CM polypeptide in the apo MtCM–MtDS

complex (PDB ID: 2W19,²¹ chain D). The malate complex was chosen over ligand-free MtCM (PDB ID: 2QBV)⁴¹ due to its higher resolution and better refinement statistics. Both simulations gave essentially the same result; therefore, we will not refer to the second data set any further. For the highly active evolved MtCM variant (MtCM^V), we used the recent crystal structure (PDB ID: SMPV).¹² The MtCM–ligand complex (MtCM^{LC}) was taken from PDB ID: 2W1A,²¹ excluding the MtDS partner protein, where MtCM was co-crystallized with a transition state analog (TSA) in its active site (Figure 1). Finally, the V55D variant was modeled based on a partially refined experimental structure (Table S1). Residues that were not fully defined were added to the models using (often weak) electron density maps as reference in Coot.³⁷ When no interpretable density was visible, geometric restraints (and α -helical restraints for residues in helix H1) were applied during model building, to ensure stable starting geometries. The N-termini of all of the models were set at Glu13, corresponding to the first defined residue in almost all of the resolved structures available. Glu13 was capped with an acetyl group to imply the continuation of the H1 helix. CM dimers were generated by 2-fold crystallographic symmetry.

Missing H-atoms were added to the model and the systems were solvated in a periodic box filled with explicit water molecules, retaining neighboring crystallographic waters, and keeping the protein at least 12 Å from the box boundaries. The systems were neutralized through the addition of Cl⁻ ions at a minimum distance of 7 Å from the protein and each other. Additional buffering moieties like glycerol or sulfate ions found in the crystals were not considered. MD simulations were run using the Gromacs 5.1.4 package^{42,43} using the AMBER 12 force fields for the protein moieties^{44,45} and the TIP3P model for water.⁴⁶ The ligand was modeled using the GAFF force field.⁴⁷ The smooth particle mesh Ewald method was used to compute long-range electrostatic interactions,⁴⁸ while a cutoff of 11 Å was used to treat the Lennard–Jones potential.

The systems were minimized using the steepest descent/conjugate gradients algorithms for 500/1500 steps until the maximum force was less than 1000 kJ mol⁻¹ nm⁻¹. To equilibrate and heat the systems, first we ran 100 ps MD in the NVT ensemble starting from a temperature of 10 K, using the canonical velocity rescaling thermostat⁴⁹ followed by 100 ps in the NpT ensemble with a Parrinello–Rahman barostat⁵⁰ targeting a final temperature of 310 K and a pressure of 1 atm. After initial equilibration, 1 μ s of MD simulation was performed for each system. In all MD simulations, the time step size was set to 2 fs.

RESULTS

The fact that MtCM exhibits only low natural catalytic activity provided us with a perfect opportunity to probe features that optimize CM catalysis by directed evolution.¹² Since the biggest gains in catalytic activity were contributed by exchanging the H1–H2 loop residues 52 (T52P) and 55 (V55D), we set out to determine the crystal structures of these two enzyme variants. Together, these two substitutions led to an increase in k_{cat}/K_m by 22-fold compared to the parent enzyme.¹²

Crystal Structures of MtCM^{T52P} and MtCM^{V55D}. Whereas MtCM^{T52P} crystals had the same space group ($P4_32_12$) and similar cell parameters as the wild-type enzyme (PDB IDs: 2VKL²¹ and 2QBV⁴¹), with one protomer in the asymmetric unit, MtCM^{V55D} crystallized in a different space group

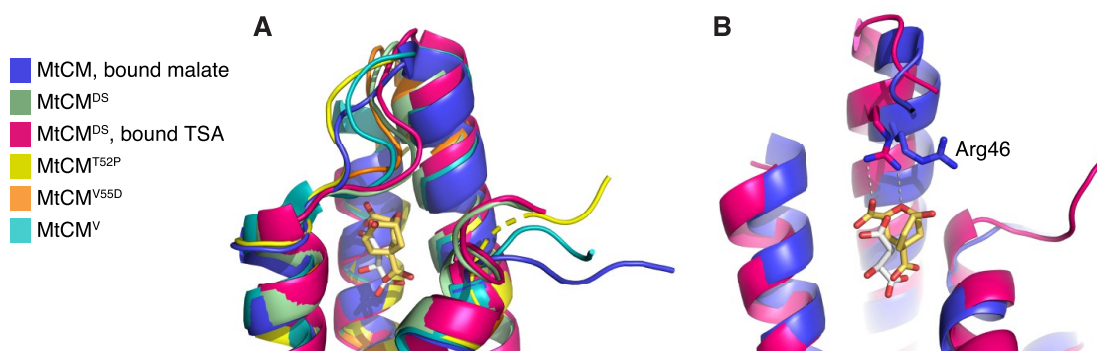


Figure 2. Comparison of MtCM crystal structures, with focus on Arg46 and H1–H2 loop. (A) Superimposition of the active site of MtCM (PDB ID: 2VKL;²¹ violet), MtCM^{DS} (PDB ID: 2W19;²¹ green), MtCM^{DS}–TSA complex (PDB ID: 2W1A;²¹ pink), MtCM^{T52P} (PDB ID: 6YGT, this work; yellow), MtCM^{V55D} (this work; orange), and top-evolved MtCM^V (PDB ID: 5MPV;¹² cyan); cartoon representation featuring the H1–H2 loop, with the ligands depicted as sticks. (B) Superimposition of MtCM (PDB ID: 2VKL;²¹ violet, with bound malate in gray sticks) and MtCM in the MtCM–MtDS complex (PDB ID: 2W1A;²¹ pink, with TSA in golden sticks, corresponding to MtCM^{LC}) in cartoon representation, with the catalytically important Arg46 depicted as sticks. MtDS binding promotes the catalytically competent conformation of Arg46. Helix H2 was removed for clarity.

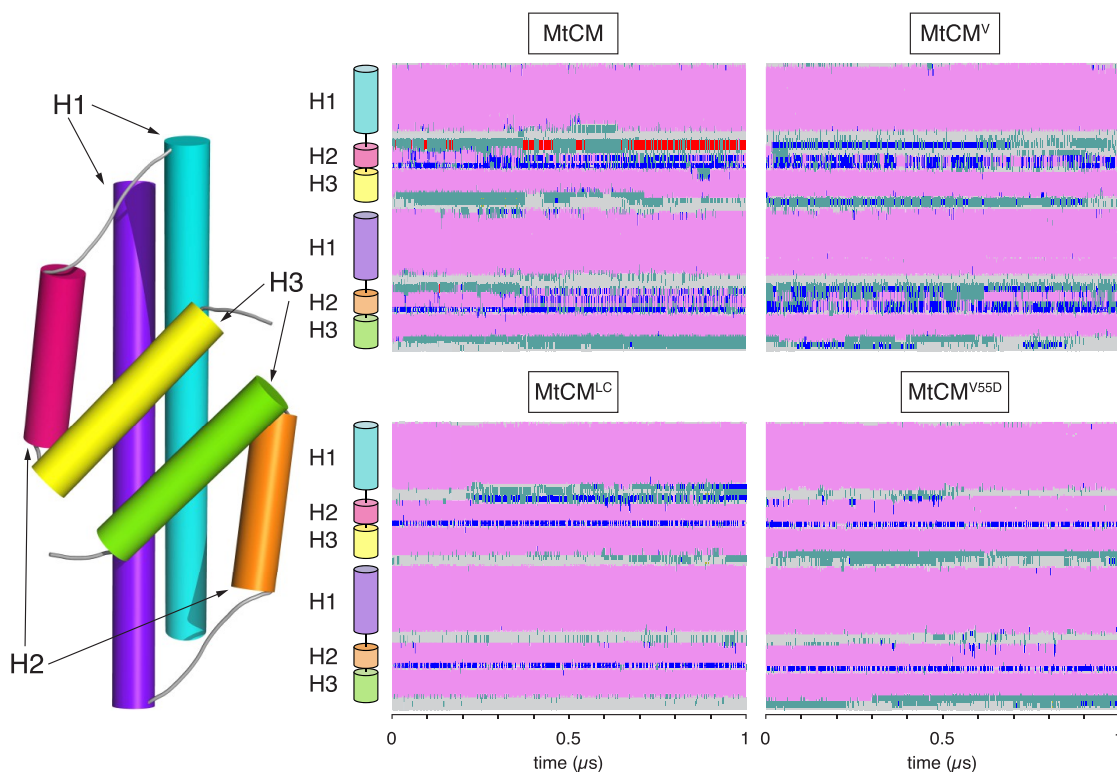


Figure 3. Secondary structure changes of MtCM during MD simulations. Estimated secondary structure of MtCM over 1 μ s of MD simulation. Color code: α -helical structure (magenta), 3_{10} helix (blue), π -helix (red), turn (green), coil (gray). The top panels report data for apo MtCM and MtCM^V, showing clear instability of H2. The bottom panels present the data for the holo-MtCM^{LC} system and for the single V55D variant (apo structure), which in contrast retained all secondary structure elements within the simulation time.

(P22₁,2₁), where the asymmetric unit contained the biological dimer. The MtCM^{T52P} structure was refined to 1.6 Å and $R_{\text{work}}/R_{\text{free}}$ values of 24.0/26.5% (Table S1 and Figure S1B), whereas MtCM^{V55D} diffraction data yielded lower-quality electron density, particularly for the H1–H2 loop (Figure S1C,D). Consistent with this, the Wilson B -factor of MtCM^{V55D} is high (57.8 Å²), indicating structural disorder. Refinement of the 2.1 Å MtCM^{V55D} model stalled at $R_{\text{work}}/R_{\text{free}}$ values of 27.6/34.9%, with very high B -factors for H1–H2 loop residues, especially for protomer B. For both structures, residues preceding residue Glu13 and C-terminal to Leu88

showed poorly defined electron density. Therefore, the terminal residues were not included in the final model.

Overall, the crystal structures of both MtCM^{T52P} (PDB ID: 6YGT) and MtCM^{V55D} are very similar to the structure of substrate-free wild-type MtCM (PDB ID: 2QBV),⁴¹ with RMSD = 0.3 and 0.4 Å, respectively. However, the H1–H2 loops (⁴⁷MASGGPRLDHS⁵⁷) of both protomers of MtCM^{V55D} adopt a different conformation (RMSD = 2.3 Å compared to PDB ID: 2QBV), which most closely resembles the kinked conformation in the MtCM–MtDS complex (PDB ID: 2W19;²¹ RMSD = 0.8 Å) (Figure 2A). In the crystal structure

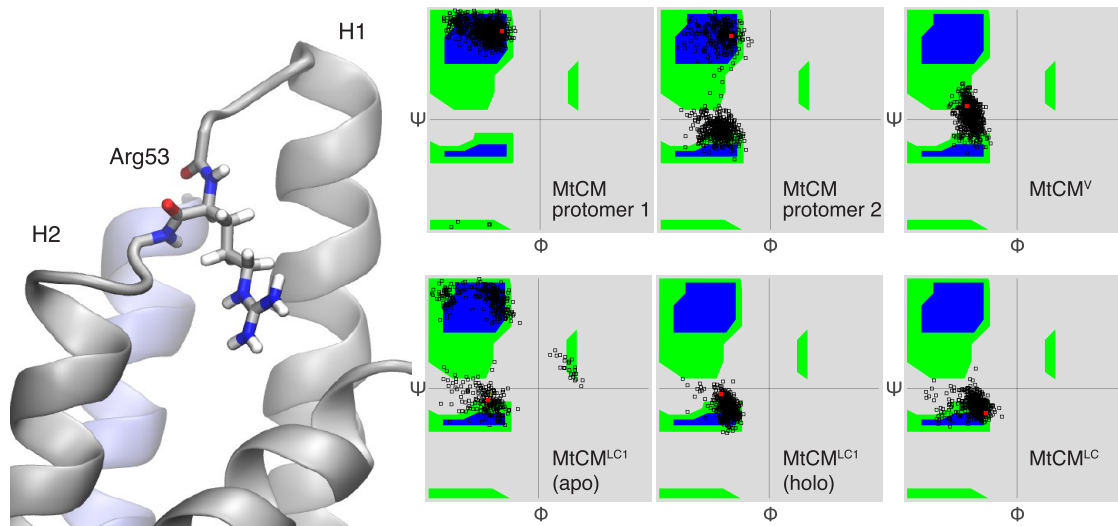


Figure 4. Conformation of Arg53 in the H1–H2 loop. Ramachandran plot showing backbone dihedral angles Φ and ψ for Arg53. Red dots mark starting conformations. For MtCM, the H1–H2 loops from the two protomers (left and middle plots in the top row) assume different ensembles of conformations; overall, the catalytically favored conformation ($\Psi \sim 0$) is observed less frequently than the nonproductive one. In contrast, in MtCM^V, both loops retained the active conformation during the entire course of the simulation, similarly to that observed for MtCM^{LC}. When only one ligand was bound (MtCM^{LC1}), the TSA-loaded site (holo) retained the active conformation, while the loop in the other protomer (apo) remained flexible.

of MtCM^{VSSD}, Asp55 in the H1–H2 loop forms a salt bridge with Arg46, similar to the one in MtCM^V (compare Figure S1E,G,H). This interaction preorganizes the active sites of both MtCM variants for catalytic activity, mimicking MtCM in the complex with MtDS (Figure 2B). However, the overall conformation of the active site loop, which is involved in extensive crystal contacts that are highly distinct for the different crystal forms (Figure S2), differs significantly between the structures (Figures S1 and 2A).

MD Simulations. To evaluate the behavior of MtCM in the absence of crystal contacts, we probed the MtCM structures by MD simulations. We used four model systems: low-activity apo wild-type MtCM, MtCM^{LC} (“ligand complex”: wild-type MtCM from the MtCM–MtDS structure in complex with TSA, the transition state analog of the CM reaction;⁵¹ Scheme 1 and Figure 1), MtCM^V, corresponding to the highly active evolved variant N-s4.15,¹² and MtCM^{VSSD}, which shows the highest catalytic activity among the single-substitution MtCM variants.¹² We compared the overall dynamic profiles of these models and inspected the interactions formed between the C-termini and the H1–H2 loops covering the active sites, to find general features that could be associated with increased catalytic competence.

Apo Structures of MtCM Are Characterized by Significant Flexibility. We anticipated that the model systems would more or less retain the same fold as observed in the crystal structures, but that regions associated with crystal contacts, like the C-termini and the H1–H2 loop, would rapidly move away from their starting positions. Instead, the MD simulations revealed large changes from the initial crystal geometries in the apo protein structures, causing a rather high root-mean-square deviation (RMSD) from the original crystal structure geometry for the CM core regions (RMSD = 2.8 ± 1.2 Å (MtCM) or 3.4 ± 1.5 Å (MtCM^V)). In particular, helix H2 showed a tendency to unravel (Figure 3). Due to the large flexibility observed, the two protomers making up the biological dimer instantaneously broke their symmetry,

independently exploring different conformations in two chains. In contrast, the ligand-bound structure MtCM^{LC} retained the secondary structure throughout the 1 μ s simulation (Figure 3), with a lower RMSD (1.7 ± 0.6 Å) than the two apo structures. Intriguingly, a similar stabilization was observed for the unliganded variant MtCM^{VSSD} (Figure 3).

Kinked Conformation of the H1–H2 Loop. One of the biggest conformational changes in the crystal structure upon formation of the MtCM–MtDS complex occurs in the H1–H2 loop (Figures 1C and 2A).²¹ Whereas in the X-ray structure of the MtDS-activated MtCM, the H1–H2 loop is strongly kinked, this is not the case in nonactivated MtCM. We investigated the conformational landscape of this loop by simulations, using Arg53 from the loop as reporter residue. As shown in Figure 4, in one of the two protomers of MtCM, Arg53 remained in an extended conformation for the entire 1 μ s MD simulation. In contrast, the same amino acid in the other protomer oscillated between the extended and the helical region of the Ramachandran plot (Figure 4), the latter being characteristic of the catalytically active conformation of the loop. Statistically averaging the two distributions, it appears that the apo form of MtCM is preferentially found in its inactive conformation, whereas in MtCM^V both protomers assumed the kinked active loop conformation, and retained it for the whole length of the simulation. However, TSA binding promoted the active conformation also in wild-type MtCM (represented by MtCM^{LC}). The fact that the fluctuations of the MtCM^V H1–H2 loop are contained within the conformational basin of the catalytically competent geometry (Figure 4 and Table 1) is an indication that MtCM^V has an intrinsically preorganized loop, a condition that helps to minimize the entropy loss during substrate binding and consequently favors catalysis.

To test the effect of ligand binding, we repeated simulations of MtCM loaded with only one TSA ligand (MtCM^{LC1}). Interestingly, ligand presence in one of the two binding pockets was sufficient to stabilize the structure of the whole

Table 1. Root-Mean-Square Fluctuation (RMSF) Values of Selected Active Site Residues^a

	RMSF (Å)			
	MtCM ^{WT}	MtCM ^V	MtCM ^{LC}	MtCM ^{VSSD}
Arg18'	2.2 ± 0.5	1.5 ± 1.0	0.7 ± 0.2	1.1 ± 0.5
Arg35	0.8 ± 0.4	0.7 ± 0.4	0.4 ± 0.1	0.6 ± 0.2
Arg46	2.0 ± 0.6	1.7 ± 0.7	0.7 ± 0.5	0.9 ± 0.5
Arg58	2.3 ± 1.0	1.9 ± 2.0	2.0 ± 0.9	1.5 ± 0.6

^aRMSF values were calculated as an average over all nonhydrogen atoms for each residue compared to the average structure of the simulation. The reported σ values reflect the different relative fluctuations of the individual atoms composing the residues in the two symmetric protomers.

dimer. Nonetheless, the H1–H2 active site loop of the apo protomer retained its intrinsic flexibility (Figure 4). The fact that the active site loop of the unloaded protomer behaved like the apo MtCM system suggests that the two active sites in MtCM retain considerable independence.

Contrary to MtCM and MtCM^V (Figure 1C,D), the presence of the additional carboxylate group in MtCM^{VSSD} promoted the elongation of helix H2, resulting in a significant shortening of the active H1–H2 loop (Figure 5A). This structural rearrangement is associated with the formation of persistent salt bridges between Asp55, now localized in the first turn of H2, and active site residues Arg18' and Arg46 that were retained for the entire length of the simulation. Noticeably, in MtCM^{WT}, where such stabilizing electrostatic interactions are absent, no such contacts were observed, with the side chain of Val55 keeping a distance of more than 10 Å from the side chains of both Arg18' and Arg46 for the whole duration of the simulation.

Overall, MtCM^{WT} shows a noisier RMSF profile over the whole amino acid sequence compared to MtCM^V and to the ligand complex MtCM^{LC} (Figure S3). This result reflects the expected rigidification occurring upon substrate binding due to additional protein–ligand interactions in MtCM^{LC}. MtCM^V accomplishes rigidification as a direct consequence of its evolved sequence. Interestingly, also MtCM^{VSSD} shows generally dampened fluctuations, possibly due to the extended helical motif observed in that structure.

Positioning of Active Site Residues. The MtCM active site contains four arginine residues (Figure 1F), among them the key catalytic residue Arg46. In contrast to the observation in the two MtCM–MtDS crystal structures, the conformation of Arg46 was not strictly maintained during MD simulations. In the absence of a ligand, Arg18', Arg46, and Arg58 repelled each other, and at least one of the residues was pushed out of the active site in the majority of the simulations. Only one of the four arginine residues (Arg35) maintained its position (Table 1), appropriately placed for substrate binding by wild-type MtCM, with an RMSF below 1 Å, while RMSF values >2 Å for the other Arg residues signal a substantial increase in the conformational freedom. This changes upon complex formation with MtDS, guiding also the important Arg46 into a catalytically competent conformation.

In contrast to MtCM^{WT}, the two variants MtCM^V and MtCM^{VSSD} exhibited lower RMSF values for all active site Arg residues (Table 1 and Figure 1F) and maintained their catalytically competent conformation during the MD simulations even in the apo forms (Figure 5). The more stable positioning of Arg18' and Arg46 appears to be a direct

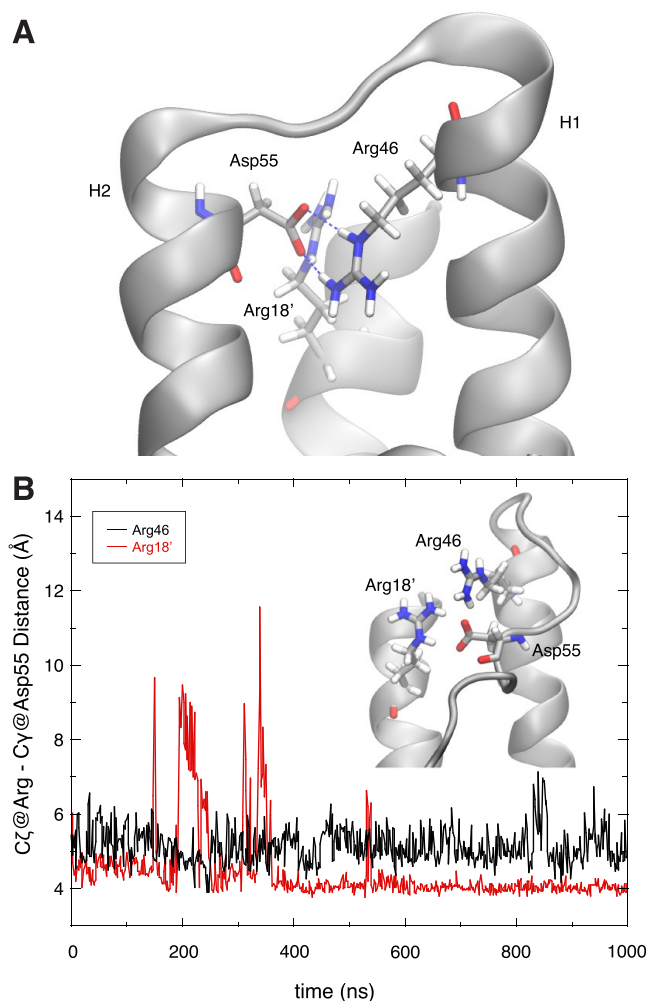


Figure 5. Role of MtCM^V residue Asp55 in positioning active site residues. (A) Extension of H2 and stabilization of the H1–H2 loop by residue Asp55. Substitution of Val55 by Asp stabilizes helix H2 through interactions with Arg18' and Arg46 across the active site (the image shows the structure of VSSD after 1 μ s of MD simulations). Note that Arg46 is a catalytically essential residue for MtCM and its correct orientation is critical for catalytic proficiency. (B) Distance plotted between MtCM^V Arg46 (black, chain A) or Arg18' (red, from chain B), and Asp55 (chain A) observed during the simulation. In both cases, the distance measured is between Asp C γ and Arg C γ using PDB nomenclature.

consequence of the replacement of Val55 with Asp, which introduces a negative charge, mitigating the surplus positive charges in the active site.

Interactions between C-Terminal Residues and H1–H2 Loop. A crucial factor for the enhanced activity of MtCM in the MtCM–MtDS complex is an MtDS-induced interaction between MtCM's H1–H2 loop and its C-terminus.²¹ The interaction can be divided into two contributions: a salt bridge between the C-terminal carboxylate and the side chain of Arg53, and a hydrophobic contact between Leu54 and Leu88 (Figure S4A).

Our 1 μ s-long simulations detected persistent, multiple interactions involving the C-terminal carboxylate. In contrast, the hydrophobic contacts between Leu54 and Leu88 were disrupted in the first nanoseconds, and almost never observed again during the rest of the simulation time (Figure S4B,C).

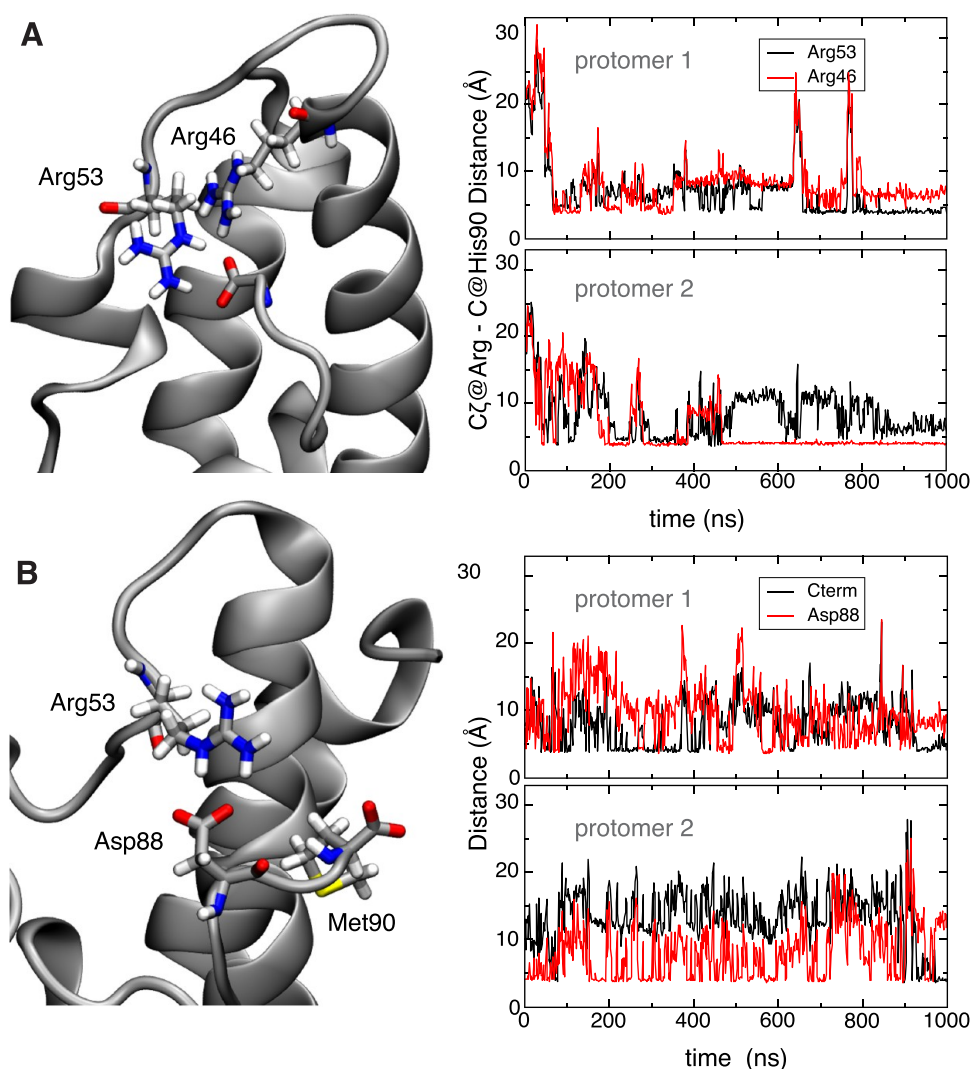


Figure 6. Interaction between C-terminal carboxylate of MtCM and H1–H2 loop. (A) Right panels show the distance between the C_γ carbon of arginine residues 53 or 46 and the carboxylate carbon of the C-terminus of MtCM in the two protomers (top and bottom panels). Formation of a steady contact (<5 Å) with Arg46 (bottom panel) corresponds to stabilization of the catalytically productive H1–H2 loop conformation, which allows for stabilization of the transition state of the chorismate to prephenate rearrangement (Figure 1B,F). (B) Interaction between C-terminal residues and the H1–H2 loop in MtCM^V. Salt bridge contacts between Arg53 and the carboxyl groups of Asp88 (red line) and Met90 (C-terminus; black line) in MtCM^V in the two protomers. The top and bottom panels on the right show the evolution of the distances over time between Arg53's C_γ and the corresponding carboxylate carbons for each of the two protomers of MtCM^V.

Salt Bridges with C-Terminus. In our MD simulations, the C-terminal carboxylate formed interchangeable contacts with Arg53 and the catalytically important Arg46,²¹ which is located in the last turn of helix H1 (Figure 6A). Notably, the presence of a salt bridge between Arg46 and the C-terminus correlated with the apparently active conformation of the H1–H2 loop (Figure 6A).

The observed fluctuations suggest that the catalytically competent conformation of the binding site is malleable in wild-type MtCM and that additional interactions, *i.e.*, with the substrate, are required to stabilize it. This is in line with studies of a topologically redesigned monomeric CM from *Methanococcus jannaschii*. This artificial enzyme was found to be catalytically active in the presence of the substrate despite showing extensive structural disorder without a ligand, reminiscent of a molten globule.⁵²

MtCM^V Exhibits Strengthened Interactions between C-Terminus and H1–H2 Loop. In MtCM^V, the four C-terminal

residues Arg–Leu–Gly–His (RLGH) are substituted with Pro–Asp–Ala–Met (PDAM) at positions 87–90, which include another carboxylate, introduced through Asp88. Our MD simulations show that the Asp88 carboxylate in the evolved variant MtCM^V offers an alternative mode of interaction with Arg53 of the H1–H2 loop (Figures 6B and S5), which is not possible for wild-type MtCM. This allows for a persistent interaction of C-terminal residues with the H1–H2 loop throughout the simulation, while maintaining a highly flexible C-terminus. Moreover, in MtCM^V, Arg46 is topologically displaced from its original position with respect to the loop and no longer able to engage in a catalytically unproductive salt bridge with the C-terminus.

Another interesting substitution, which emerged within the four C-terminal residues during the laboratory evolution toward variant MtCM^V, is a proline residue (RLGH to PDAM).¹² However, in contrast to Pro52, Pro87 did not appear to have a major influence on the simulations. While

Table 2. Catalytic CM Activities of Purified MtCM Variants to Experimentally Address the Importance of the Leu88 to Asp88 Substitution that Emerged during the Directed Evolution of MtCM^V

Variant	Residue changes	k_{cat} (s ⁻¹) ^a	K_{m} (μM) ^a	$k_{\text{cat}}/K_{\text{m}}$ (M ⁻¹ s ⁻¹) ^a
MtCM ^V (PDAM)	PD/PDAM ^b , V62I, D72V, V11L, D15V, K40Q	9.4 ± 1.3	22 ± 2	430,000 ± 30,000
MtCM PNAM	MtCM ^V , D88N	7.6 ± 0.2	45 ± 7	170,000 ± 20,000
MtCM PLAM	MtCM ^V , D88L	6.0 ± 0.4	38 ± 1	160,000 ± 10,000
MtCM ^{WTc}		1.7 ± 0.2	980 ± 80	1700 ± 300
MtCM L88D ^c	L88D	3.0 ± 0.1	1110 ± 70	2700 ± 300
MtCM 3p3	T52P V55D	8.5 ± 0.0	450 ± 70	19,000 ± 3000
MtCM Triple	T52P V55D L88D	11 ± 2	510 ± 130	22,000 ± 1000

^aAll values are experimental means from assays performed with at least two independently produced and purified protein batches with their calculated standard deviations (σ_{n-1}). The $k_{\text{cat}}/K_{\text{m}}$ parameters were obtained as the mean from averaging $k_{\text{cat}}/K_{\text{m}}$ values derived directly from individually fitted independent Michaelis–Menten plots with the calculated error of the corresponding average. ^bPD/PDAM indicates amino acid substitutions T52P, V55D, R87P, L88D, G89A, and H90M. ^cThe default for measuring kinetics involved assays performed in 50 mM K-phosphate, pH 7.5, at 274 nm, whereas the kinetic parameters of these low-performing variants were determined in 50 mM BTP, pH 7.5, at 310 nm. Measuring these variants in 50 mM K-phosphate, pH 7.5, resulted in ~40% reduction in k_{cat} , as was already observed previously for wild-type MtCM.²¹

Pro52 is likely contributing to H1–H2 loop rigidity, with an average RMSF of 1.6 Å in MtCM^V compared to 2.5 Å (MtCM) for this region, the C-termini showed similarly high RMSF values in the two models (>3 Å). Although Pro87 induced a kink at the C-terminus, this did not appear to affect the flexibility of the three terminal residues Asp88–Ala89–Met90.

Kinetic Analysis to Probe Predicted Key Interactions of Engineered MtCM Variants. In the course of the directed evolution of MtCM^V, the L88D replacement was only acquired after the H1–H2 loop-stabilizing substitutions T52P and V55D were already introduced. Guided by the outcome of the MD simulations, we therefore probed the kinetic impact of the innocuous single L88D exchange in the context of three different sets of MtCM variants to experimentally assess the benefit of the introduced negative charge for fine-tuning and optimizing catalytic efficiency. We looked at (i) changing Asp88 in the MtCM^V sequence ⁸⁷PDAM⁹⁰ into Asn88 or Leu88, (ii) directly introducing Asp88 into the MtCM wild-type sequence, and (iii) the triple variant T52P V55D L88D (MtCM Triple). All variants were obtained in their native format, *i.e.*, with their native N-terminus and without a His-tag, to allow for optimal comparison with the structural and computational results. The variants were purified by ion-exchange and size-exclusion chromatography from the *E. coli* host strain KA13, which is devoid of CM genes to rule out contamination by endogenous CMs.^{18,30} Subsequently, the enzymes' kinetic parameters were characterized by a spectrophotometric chorismate depletion assay.

As shown in Table 2, removing the negative charge at residue 88 by replacing Asp with Asn in the top-evolved variant MtCM^V leads to a 2.5-fold drop in the catalytic efficiency $k_{\text{cat}}/K_{\text{m}}$ to $1.7 \times 10^5 \text{ M}^{-1} \text{ s}^{-1}$. This decrease is due both to a slightly lower catalytic rate constant (k_{cat}) as well as a reduced substrate affinity (doubled K_{m}). When residue 88 is further changed to the similarly sized but nonpolar wild-type residue Leu88 in variant MtCM PLAM, the catalytic parameters essentially remain the same as for the Asn88 variant (Table 2), independently confirming the catalytic advantage of the negative charge introduced through Asp88.

For the second set of variants that directly started out from the sluggish MtCM wild-type enzyme (MtCM^{WT}), a trend for an increase in catalytic activity upon replacing Leu88 by Asp88 was observed (1.6-fold higher $k_{\text{cat}}/K_{\text{m}}$, reaching $2.7 \times 10^3 \text{ M}^{-1} \text{ s}^{-1}$; Table 2). This is mainly caused by an increase in k_{cat} rather

than an altered substrate affinity. Interestingly, the L88D exchange together with T52P and V55D in the MtCM triple variant does not lead to a significant increase in $k_{\text{cat}}/K_{\text{m}}$ compared to MtCM 3p3,¹² which just carries the two loop substitutions T52P and V55D.

Thus, the substitution of Leu88 with Asp88 indeed results in a beneficial effect on the performance of MtCM. However, this effect is only prominent in combination with other selected exchanges, such as those present in MtCM^V. As a single amino acid replacement in the wild-type enzyme or on top of the two substitutions in the H1–H2 loop, the effect of L88D is less noticeable, if present at all.

In summary, a comparison of the dynamic behavior of wild-type MtCM in its apo and ligand-bound states with MtCM^V and MtCM^{V55D} revealed that the catalytically favorable conformation of the active site is achieved by the interplay of several interactions, which balance charges and entropic disorder of the H1–H2 loop. Structuring is promoted, in particular, by increasing the number of the negatively charged carboxylate groups that can both shield the electrostatic charge of the various arginine side chains within or next to the active site and orient catalytically important residues by hydrogen bonding and salt bridge formation. Simulations of MtCM^V revealed the special importance of Asp55 in the V55D variant for coordinating Arg18' and Arg46, thus promoting the preorganization of the active site region. These results echo the conclusions from directed evolution, which also identified the V55D substitution as the most important contributor for catalytic enhancement, causing a 12-fold increase in $k_{\text{cat}}/K_{\text{m}}$.¹² At the same time, we determined and rationalized the more subtle and context-dependent effect of the L88D replacement that introduced an additional negative charge for electrostatic preorganization of the active site. Overall, the high catalytic activity of MtCM^V clearly results from many individual larger and smaller contributions mediated by substitutions at diverse locations within the enzyme structure.

DISCUSSION

Important Activating Factors in MtCM^{DS} and MtCM^V. MtCM has intrinsically low activity but can be activated to rival the performance of the best CMs known to date¹² through the formation of a heterooctameric complex with MtDS,²¹ which aligns crucial active site residues to catalytically competent conformations. Most importantly, binding to MtDS induces preorganization of Arg46 into a catalytically favorable

conformation (Figure 2B), via H-bonding to the carbonyl oxygens of Thr52 and Arg53.²¹ Arg46 is the crucial catalytic residue interacting with the ether oxygen of Bartlett's transition state analogue (TSA)⁵¹ in the complex with MtDS (PDB ID: 2W1A)²¹ (Figures 1B,F and 2B); upon replacing Arg with Lys, the enzyme's efficiency drops 50-fold.²¹

Both MtCM^{DS} and MtCM^V exhibit a kinked H1–H2 loop conformation (Figures 1C,D and 2A), which was hypothesized to be important for increased catalytic efficiency.¹² However, in MtCM^V and MtCM^{V55D}, the kink is exacerbated by crystal contacts, which are different in the two crystal forms (Figure S2). This kink is much less prominent in wild-type MtCM, or even MtCM^{T52P} (Figures 2A and S1B), and completely lost during the simulations of MtCM^{WT} (we did not carry out simulations on the single variant MtCM^{T52P}). Thus, this conformation may well be a crystallization artifact rather than a prerequisite for an active MtCM.

Nevertheless, preorganization and prestabilization appear to be of crucial importance for the catalytic prowess of MtCM. The largest boost in catalytic efficiency (12-fold enhancement) by a single substitution was observed for the V55D replacement found in the evolved MtCM^V.¹² This residue is located on the C-terminal side of the H1–H2 loop (Figure 1D,E) and forms a salt bridge to the catalytically important Arg46 at the top of helix H1 (Figure 5A), an interaction that is also observed in the crystal structure of MtCM^{V55D} (Figure S1G,H). During the MD simulations of MtCM^V and the single variant MtCM^{V55D}, the presence of Asp55 reduced the mobility of active site residues. By interacting with Arg18' and Arg46, this residue helps to preorganize the active site for catalysis and reduce unfavorable conformational fluctuations caused by electrostatic repulsion in the absence of a substrate. This is supported by the lower RMSF values of MtCM^V compared to uncomplexed wild-type MtCM (Table 1) and by a slightly higher melting temperature of MtCM^{V55D} ($\Delta T = 3$ °C from differential scanning fluorimetry (DSF) measurements; preliminary data). By decreasing thermal fluctuations in the active site, Asp55 likely also reduces the entropic penalty associated with substrate binding. Pro52 appears to exert a similar stabilizing effect on the protein, despite the rather small structural changes, as suggested by a 2 °C increase in melting temperature of MtCM^{T52P} in DSF experiments compared to MtCM (preliminary data). This single substitution alone raises the $k_{\text{cat}}/K_{\text{m}}$ value of the enzyme by a factor of six.¹² It is worth noting that the simultaneous substitution of T52P and V55D increased the melting temperature by 6 °C (monitored by circular dichroism spectroscopy) and boosted $k_{\text{cat}}/K_{\text{m}}$ by 22-fold.¹² The top-evolved MtCM^V even showed a melting temperature of 83 °C compared to 74 °C for the parent MtCM.¹²

Importance of the C-Terminus. MtCM activation by MtDS involves a change in conformation of the C-terminus of MtCM and its active site H1–H2 loop.²¹ Specifically, a salt bridge is formed between the C-terminal carboxylate of MtCM (which is repositioned upon MtDS binding) and loop residue Arg53, possibly bolstered by a newly formed hydrophobic interaction between Leu88 and Leu54 (Figure S4A). The 1 μs simulations suggest that salt bridge formation with Arg53 occurs in solution in all tested cases, whereas the hydrophobic contact is less important.

Directed evolution experiments carried out by randomizing the final four C-terminal positions 87–90 of MtCM had previously revealed that a great variety of residues with quite

distinct physico-chemical properties are compatible with a functional catalytic machinery.²⁶ Conserved positions emerged only when probing for an intact activation mechanism by MtDS.²⁶ Still, when residues 87–90 of MtCM^V were evolved from Arg–Leu–Gly–His to Pro–Asp–Ala–Met (Figure 1E), an increase in $k_{\text{cat}}/K_{\text{m}}$ by roughly a factor of four was achieved.¹² Here, we resolved this apparent paradox by investigating C-terminal factors important for the fine-tuned optimization of CM function. Even though the replacement R87P induced a kink in the structure, the presence of the proline did not appear to have a major influence in the simulations. Notably, the C-terminal substitutions together result in a change in net charge from +1 to –2, including the terminal carboxylate, providing the basis for more extensive electrostatic interactions with the positively charged Arg53 than is possible for wild-type MtCM. Indeed, our kinetic analysis of Asp88-containing MtCM variants demonstrates that this residue increases CM's catalytic efficiency (Table 2). The fact that Asp88 did not significantly augment $k_{\text{cat}}/K_{\text{m}}$ in the context of the MtCM double variant T52P V55D (*i.e.*, MtCM Triple; Table 2) suggests that the extent of catalytic improvement by L88D depends on the particular structural context.

Our simulations indicate that in free wild-type MtCM, an interaction of the C-terminal carboxylate with the key active site residue Arg46 is possible but infrequent due to fluctuations (Figure 6A and Table 1). In contrast, in MtCM^V and MtCM^{DS} the side chain of Arg46 points toward the catalytic pocket (Figures 5 and 2B), and any unproductive reorientation of Arg46 toward the C-terminus would easily result in a clash with the H1–H2 loop. Thus, an additional feature of this loop may be to act as a conditional shield (illustrated for MtCM^V in Figure 7). In the conformation assumed in MtCM^V and MtCM^{DS}, this loop blocks the reorientation of Arg46 toward the C-terminus and hence prevents an unproductive conformation accessible for free wild-type MtCM. MtCM^{DS} and MtCM^V use different means to correctly position active site residues, which correlates with a bent H1–H2 loop in both cases. This is either achieved through conformational changes imposed upon MtCM^{DS} by MtDS binding, or by establishing a salt bridge across the active site, between Arg46 and Asp55, as seen for MtCM^V and also for the single variant MtCM^{V55D} (Figures 5 and S1E,G,H).

General Implications for CM Catalysis. It is obviously impossible to directly transfer our findings of critical detailed molecular contacts from the AroQ _{δ} subclass CM of *M. tuberculosis* to the evolutionary distinct AroH class CMs, or even to the structurally and functionally divergent AroQ _{α} , AroQ _{β} , and AroQ _{γ} subclasses.⁵³ Neither of those groups of CMs have evolved to be deliberately poor catalysts that become proficient upon regulatory interaction with a partner protein such as MtDS.²¹ To be amenable to 'inter-enzyme allosteric' regulation,²⁸ the H1–H2 loop in MtCM must be malleable and allow for conformational switching between a poorly and a highly active form. In contrast, this region is rigidified in a catalytically competent conformation in the overwhelming majority of CMs from other subclasses. This is exemplified by the prototypic EcCM (AroQ _{α} subclass) and the secreted *MtCM (AroQ _{γ}), which possess the sequence ⁴⁵PVRD⁴⁸ and ⁶⁶PIED⁶⁹, respectively, at the position corresponding to the malleable H1–H2 loop sequence ⁵²TRLV⁵⁵ of wild-type MtCM.¹² Remarkably, the two most impactful substitutions T52P and V55D occurring during the

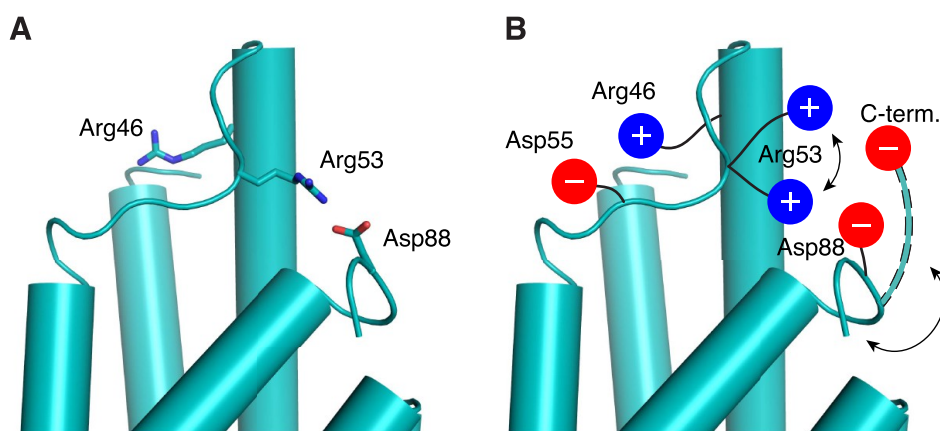


Figure 7. Shielding interaction mediated by the H1–H2 loop. (A) Conformation of important Arg residues in chain A of MtCM^V (cyan) after 31.7 ns of MD simulations. The key active site residue Arg46 is positioned on the opposite side of the H1–H2 loop, which in turn is bolted to the C-terminus by a salt bridge between Arg53 and Asp88 (cartoon representation, with side chains shown as sticks). (B) Cartoon summarizing the important stabilizing interactions in the top-evolved variant MtCM^V depicted in (A) that properly position Arg46 for catalysis. Asp55 stabilizes the stretched-out conformation of Arg46, whereas alternating salt bridges accessible for Arg53 with the negatively charged groups present in the C-terminal region hinder Arg46 from adopting an unfavorable interaction with the C-terminal carboxylate. One example of an alternative backbone conformation that allows for interactions between the C-terminal carboxylate and Arg53 is depicted with dashed outlines.

evolution of MtCM^V have led to the tetrapeptide sequence ⁵²PRLD⁵⁵, with both Pro and Asp being conserved in naturally highly active CMs.¹²

The AroQ₅ subclass CM from *Corynebacterium glutamicum* is another structurally well-characterized poorly active CM ($k_{\text{cat}}/K_{\text{m}} = 110 \text{ M}^{-1} \text{ s}^{-1}$) that requires complex formation with its cognate DAHP synthase for an impressive 180-fold boost in catalytic efficiency.⁵⁴ In that case, inter-enzyme allosteric regulation involves a conformational change of a different malleable segment between helices H1 and H2. Thus, while the molecular details important for the activation of a particular AroQ₅ CM cannot be transferred directly from one system to another, our findings suggest as a general regulatory principle the deliberate and reversible destabilization of a catalytically critical loop conformation.

In both the *M. tuberculosis*¹² and the *C. glutamicum* systems,⁵⁴ crystal contacts in the H1–H2 loop region impede the structural interpretation of the activity switching. The MD simulations shown here represent an interesting alternative approach to dynamic high-resolution structure determination methods for sampling the conformational space adopted by malleable peptide segments with and without ligands.

CONCLUSIONS

MD greatly aided the analysis of crystal structures that were compromised or biased by extensive crystal contacts at the most interesting structural sites. Our aim was to obtain insight into the crucial factors underlying CM activity by comparing the structure and dynamics of the poorly active wild-type MtCM ($k_{\text{cat}}/K_{\text{m}} = 1.7 \times 10^3 \text{ M}^{-1} \text{ s}^{-1}$) with the top-performing MtCM variant MtCM^V ($k_{\text{cat}}/K_{\text{m}} = 4.3 \times 10^5 \text{ M}^{-1} \text{ s}^{-1}$), which emerged from directed evolution experiments. Both in MtDS-activated wild-type MtCM and in MtCM^V, high activity correlated with a kinked H1–H2 loop conformation and an interaction of this region with the C-terminus of MtCM. The autonomously fully active variant MtCM^V had amino acid changes in both of these regions that augment these structural features. In this report, we focussed on substitutions T52P, V55D, and L88D.

The active site of all natural CMs contains a high density of positive charges. In MtCM, four arginine residues (Arg18', Arg35, Arg46, and Arg58, of which Arg18' is contributed by a different MtCM protomer) are responsible for binding and rearranging the doubly negatively charged substrate chorismate. Only one of these residues (Arg35) is firmly in position before the substrate enters the active site. Of critical importance for catalysis is Arg46. During the MD simulations, Arg46 competes with another arginine residue (Arg53) for binding to the C-terminal carboxylate (Figure 6A) and adopts a catalytically unproductive conformation unless an aspartate residue (Asp55 or Asp88) comes to its rescue. As shown here, Asp55 not only properly orients Arg46 for catalysis but additionally stabilizes the active site. Together with T52P, which preorders the H1–H2 loop, the V55D exchange results in reduced mobility of residues in the active site through stabilizing interactions, thereby preorganizing it for efficient catalysis and lowering the entropic cost of substrate binding. Another aspartate residue (Asp88), also acquired in the top-evolved MtCM^V,¹² helps to balance charges, and—by interacting with Arg53—imposes a steric block that prevents nonoptimal positioning of Arg46 (Figure 7), explaining why the L88D exchange can increase $k_{\text{cat}}/K_{\text{m}}$ by about 2- to 3-fold.

In summary, we tested our hypotheses on the specific importance of critical substitutions acquired during the directed evolution of MtCM^V, namely, T52P, V55D, and L88D by investigating single variants as well as combinations with other residue replacements that were found to augment catalysis. The variants were characterized by crystallography, MD simulations, and enzyme kinetics. The two residues Pro52 and Asp55 exert a major impact by prestabilization and preorganization of catalytically competent conformations of active site residues, while Asp88 contributes to fine-tuning and optimizing the catalytic process. By expanding on the previous directed evolution studies, we have shown here how the accumulated set of amino acid substitutions found in MtCM^V has resulted in an activity level matching that of the most active CMs known to date.¹²

■ ASSOCIATED CONTENT

SI Supporting Information

The Supporting Information is available free of charge at <https://pubs.acs.org/doi/10.1021/acs.biochem.2c00635>.

Crystal structures and electron density maps shown for catalytically important regions (Figure S1); crystal contacts of the H1–H2 loop (Figure S2); root-mean-square fluctuations of MtCM during MD simulations (Figure S3); interactions in MtCM between its C-terminus and H1–H2 loop (Figure S4); MD snapshots of interactions between C-terminus and H1–H2 loop of MtCM^V (Figure S5); and data collection and refinement statistics (Table S1) (PDF)

Accession Codes

UniProt ID: P9WIC1 (Gene Rv0948c). PDB ID: 6YGT.

■ AUTHOR INFORMATION

Corresponding Authors

Peter Kast – Laboratory of Organic Chemistry, ETH Zürich, CH-8093 Zürich, Switzerland; orcid.org/0000-0002-0209-8975; Email: kast@org.chem.ethz.ch

Michele Cascella – Department of Chemistry and Hylleraas Centre for Quantum Molecular Sciences, University of Oslo, Oslo 0315 NO, Norway; orcid.org/0000-0003-2266-5399; Email: michele.cascella@kjemi.uio.no

Ute Krengel – Department of Chemistry and Hylleraas Centre for Quantum Molecular Sciences, University of Oslo, Oslo 0315 NO, Norway; orcid.org/0000-0001-6688-8151; Email: ute.krengel@kjemi.uio.no

Authors

Helen V. Thorbjørnsrud – Department of Chemistry and Hylleraas Centre for Quantum Molecular Sciences, University of Oslo, Oslo 0315 NO, Norway

Luca Bressan – Laboratory of Organic Chemistry, ETH Zürich, CH-8093 Zürich, Switzerland

Tamjidmaa Khatanbaatar – Department of Chemistry and Hylleraas Centre for Quantum Molecular Sciences, University of Oslo, Oslo 0315 NO, Norway

Manuel Carrer – Department of Chemistry and Hylleraas Centre for Quantum Molecular Sciences, University of Oslo, Oslo 0315 NO, Norway

Kathrin Würth-Roderer – Laboratory of Organic Chemistry, ETH Zürich, CH-8093 Zürich, Switzerland; orcid.org/0000-0002-0233-9863

Gabriele Cordara – Department of Chemistry and Hylleraas Centre for Quantum Molecular Sciences, University of Oslo, Oslo 0315 NO, Norway; orcid.org/0000-0001-8029-8043

Complete contact information is available at:

<https://pubs.acs.org/10.1021/acs.biochem.2c00635>

Author Contributions

^{||}H.V.T., L.B., and T.K. contributed equally to this work.

Author Contributions

U.K. conceived the study. H.V.T., P.K., and Mi.C. were additionally involved in the planning of the experiments. H.V.T. performed most of the calculations, transformed, produced, purified, and crystallized the two single MtCM variants, and solved the crystal structure of MtCM^{V55D}, supervised by Mi.C. and U.K., respectively. Ma.C. contributed with additional simulations, supervised by Mi.C. T.K. solved

the crystal structure of MtCM^{T52P} and refined the crystal structures of both MtCM variants, supervised by G.C. and U.K., who also validated the structures. L.B. constructed, produced, and purified additional sets of MtCM variants and characterized their kinetic parameters to validate computational results, and K.W.-R. designed and constructed the MtCM variants T52P and V55D and prepared the final figures; both were supervised by P.K. The initial version of the manuscript was written by H.V.T. and U.K., which was complemented with contributions from all authors and revised by P.K., Mi.C., and U.K.

Funding

This work was funded by grants from the Swiss National Science Foundation to P.K. (grant 310030M_182648), the Norwegian Research Council (grants 247730 and 245828), and CoE Hylleraas Centre for Quantum Molecular Sciences (grant 262695), and through the Norwegian Supercomputing Program (NOTUR) (grant NN4654K). The work was additionally supported through funds from the University of Oslo (position of H.V.T.).

Notes

The authors declare no competing financial interest.

■ ACKNOWLEDGMENTS

The authors thank Regula Grüninger-Stössel for help with the construction of the T52P and V55D variants of MtCM, and Joel B. Heim for collecting X-ray data for MtCM^{T52P}. The experiments were performed on beamlines ID30A-3/MASSIF-3 and ID29 at the European Synchrotron Radiation Facility (ESRF), Grenoble, France. We are grateful to Montserrat Soler Lopez and Daniele De Sanctis at the ESRF for providing assistance in using beamlines ID30A-3/MASSIF-3 and ID29, respectively. Finally, they acknowledge services provided by the MoBIAS facility, Laboratory of Organic Chemistry, ETH Zurich, and by the UiO Structural Biology Core Facilities.

■ ABBREVIATIONS

BTP, 1,3-bis[tris(hydroxymethyl)methylamino]propane; CM, chorismate mutase; DAHP, 3-deoxy-D-arabino-heptulosonate 7-phosphate; IPTG, isopropyl-β-D-thiogalactopyranoside; LC, ligand complex (*i.e.*, complex with TSA); MD, molecular dynamics; MES, 2-(N-morpholino)ethanesulfonic acid; MtCM, chorismate mutase from *M. tuberculosis*; MtCM^{DS}, MtCM from MtCM–MtDS complex; MtCM^{LC}, TSA-bound MtCM from MtCM–MtDS complex (LC1 refers to only one of the protomers containing TSA); MtCM^{T52P}, MtCM variant T52P; MtCM^V, top-performing MtCM variant N-s4.15 from directed evolution study; MtCM Triple, MtCM variant with the three substitutions T52P, V55D, and L88D; MtCM^{V55D}, MtCM variant V55D; MtCM^{WT}, wild-type MtCM; MtDS, DAHP synthase from *M. tuberculosis*; MWCO, molecular weight cutoff; pI, isoelectric point; PMSF, phenylmethanesulfonyl fluoride; RMSD, root-mean-square deviation (or root-mean-square difference, if concerning structural comparisons); RMSF, root-mean-square fluctuation; SDS-PAGE, sodium dodecyl sulfate polyacrylamide gel electrophoresis; Tris, tris(hydroxymethyl)aminomethane; TSA, transition state analogue

■ REFERENCES

(1) Ohashi, M.; Liu, F.; Hai, Y.; Chen, M.; Tang, M.-C.; Yang, Z.; Sato, M.; Watanabe, K.; Houk, K. N.; Tang, Y. SAM-dependent

- enzyme-catalysed pericyclic reactions in natural product biosynthesis. *Nature* **2017**, *549*, 502–506.
- (2) Minami, A.; Oikawa, H. Recent advances of Diels-Alderaes involved in natural product biosynthesis. *J. Antibiot.* **2016**, *69*, 500–506.
- (3) Tang, M.-C.; Zou, Y.; Watanabe, K.; Walsh, C. T.; Tang, Y. Oxidative cyclization in natural product biosynthesis. *Chem. Rev.* **2017**, *117*, 5226–5333.
- (4) Lin, C.-I.; McCarty, R. M.; Liu, H.-W. The enzymology of organic transformations: A survey of name reactions in biological systems. *Angew. Chem., Int. Ed.* **2017**, *56*, 3446–3489.
- (5) Sogo, S. G.; Widlanski, T. S.; Hoare, J. H.; Grimshaw, C. E.; Berchtold, G. A.; Knowles, J. R. Stereochemistry of the rearrangement of chorismate to prephenate: Chorismate mutase involves a chair transition state. *J. Am. Chem. Soc.* **1984**, *106*, 2701–2703.
- (6) Bentley, R. The shikimate pathway - A metabolic tree with many branches. *Crit. Rev. Biochem. Mol. Biol.* **1990**, *25*, 307–384.
- (7) Herrmann, K. M.; Weaver, L. M. The shikimate pathway. *Annu. Rev. Plant Physiol. Plant Mol. Biol.* **1999**, *50*, 473–503.
- (8) Lamb, A. L. Pericyclic reactions catalyzed by chorismate-utilizing enzymes. *Biochemistry* **2011**, *50*, 7476–7483.
- (9) Copley, S. D.; Knowles, J. R. The uncatalyzed Claisen rearrangement of chorismate to prephenate prefers a transition state of chairlike geometry. *J. Am. Chem. Soc.* **1985**, *107*, 5306–5308.
- (10) Wiest, O.; Houk, K. N. Stabilization of the transition state of the chorismate-prephenate rearrangement: An *ab initio* study of enzyme and antibody catalysis. *J. Am. Chem. Soc.* **1995**, *117*, 11628–11639.
- (11) Burschowsky, D.; Krengel, U.; Uggerud, E.; Balcells, D. Quantum chemical modeling of the reaction path of chorismate mutase based on the experimental substrate/product complex. *FEBS Open Bio* **2017**, *7*, 789–797.
- (12) Fahrigr-Kamaraukaitė, J.; Würth-Roderer, K.; Thorbjørnsrud, H. V.; Mailand, S.; Krengel, U.; Kast, P. Evolving the naturally compromised chorismate mutase from *Mycobacterium tuberculosis* to top performance. *J. Biol. Chem.* **2020**, *295*, 17514–17534.
- (13) Chook, Y. M.; Ke, H.; Lipscomb, W. N. Crystal structures of the monofunctional chorismate mutase from *Bacillus subtilis* and its complex with a transition state analog. *Proc. Natl. Acad. Sci. U.S.A.* **1993**, *90*, 8600–8603.
- (14) Chook, Y. M.; Gray, J. V.; Ke, H.; Lipscomb, W. N. The monofunctional chorismate mutase from *Bacillus subtilis*. Structure determination of chorismate mutase and its complexes with a transition state analog and prephenate, and implications for the mechanism of the enzymatic reaction. *J. Mol. Biol.* **1994**, *240*, 476–500.
- (15) Xue, Y.; Lipscomb, W. N.; Graf, R.; Schnappauf, G.; Braus, G. The crystal structure of allosteric chorismate mutase at 2.2-Å resolution. *Proc. Natl. Acad. Sci. U.S.A.* **1994**, *91*, 10814–10818.
- (16) Lee, A. Y.; Karplus, P. A.; Ganem, B.; Clardy, J. Atomic structure of the buried catalytic pocket of *Escherichia coli* chorismate mutase. *J. Am. Chem. Soc.* **1995**, *117*, 3627–3628.
- (17) Sträter, N.; Schnappauf, G.; Braus, G.; Lipscomb, W. N. Mechanisms of catalysis and allosteric regulation of yeast chorismate mutase from crystal structures. *Structure* **1997**, *5*, 1437–1452.
- (18) MacBeath, G.; Kast, P.; Hilvert, D. A small, thermostable, and monofunctional chorismate mutase from the archaeon *Methanococcus jannaschii*. *Biochemistry* **1998**, *37*, 10062–10073.
- (19) Calhoun, D. H.; Bonner, C. A.; Gu, W.; Xie, G.; Jensen, R. A. The emerging periplasm-localized subclass of AroQ chorismate mutases, exemplified by those from *Salmonella typhimurium* and *Pseudomonas aeruginosa*. *Genome Biol.* **2001**, *2*, 1–16.
- (20) Ökvist, M.; Dey, R.; Sasso, S.; Grahn, E.; Kast, P.; Krengel, U. 1.6 Å crystal structure of the secreted chorismate mutase from *Mycobacterium tuberculosis*: Novel fold topology revealed. *J. Mol. Biol.* **2006**, *357*, 1483–1499.
- (21) Sasso, S.; Ökvist, M.; Roderer, K.; Gamper, M.; Codoni, G.; Krengel, U.; Kast, P. Structure and function of a complex between chorismate mutase and DAHP synthase: Efficiency boost for the junior partner. *EMBO J.* **2009**, *28*, 2128–2142.
- (22) Lee, A. Y.; Stewart, J. D.; Clardy, J.; Ganem, B. New insight into the catalytic mechanism of chorismate mutases from structural studies. *Chem. Biol.* **1995**, *2*, 195–203.
- (23) Kast, P.; Asif-Ullah, M.; Jiang, N.; Hilvert, D. Exploring the active site of chorismate mutase by combinatorial mutagenesis and selection: The importance of electrostatic catalysis. *Proc. Natl. Acad. Sci. U.S.A.* **1996**, *93*, 5043–5048.
- (24) Kast, P.; Grisostomi, C.; Chen, I. A.; Li, S.; Krengel, U.; Xue, Y.; Hilvert, D. A strategically positioned cation is crucial for efficient catalysis by chorismate mutase. *J. Biol. Chem.* **2000**, *275*, 36832–36838.
- (25) Burschowsky, D.; van Eerde, A.; Ökvist, M.; Kienhöfer, A.; Kast, P.; Hilvert, D.; Krengel, U. Electrostatic transition state stabilization rather than reactant destabilization provides the chemical basis for efficient chorismate mutase catalysis. *Proc. Natl. Acad. Sci. U.S.A.* **2014**, *111*, 17516–17521.
- (26) Roderer, K.; Neuenschwander, M.; Codoni, G.; Sasso, S.; Gamper, M.; Kast, P. Functional mapping of protein-protein interactions in an enzyme complex by directed evolution. *PLoS One* **2014**, *9*, No. e116234.
- (27) Blackmore, N. J.; Nazmi, A. R.; Hutton, R. D.; Webby, M. N.; Baker, E. N.; Jameson, G. B.; Parker, E. J. Complex formation between two biosynthetic enzymes modifies the allosteric regulatory properties of both: An example of molecular symbiosis. *J. Biol. Chem.* **2015**, *290*, 18187–18198.
- (28) Munack, S.; Roderer, K.; Ökvist, M.; Kamaraukaitė, J.; Sasso, S.; van Eerde, A.; Kast, P.; Krengel, U. Remote control by inter-enzyme allostery: A novel paradigm for regulation of the shikimate pathway. *J. Mol. Biol.* **2016**, *428*, 1237–1255.
- (29) Sambrook, J.; Russel, D. W. *Molecular Cloning: A Laboratory Manual*, 3rd ed.; Cold Spring Harbor Laboratory Press: New York, 2001.
- (30) MacBeath, G.; Kast, P. UGA read-through artifacts—When popular gene expression systems need a pATCH. *Biotechniques* **1998**, *24*, 789–794.
- (31) Bradford, M. M. A rapid and sensitive method for the quantitation of microgram quantities of protein utilizing the principle of protein-dye binding. *Anal. Biochem.* **1976**, *72*, 248–254.
- (32) Kabsch, W. Integration, scaling, space-group assignment and post-refinement. *Acta Crystallogr. D Biol. Crystallogr.* **2010**, *66*, 133–144.
- (33) Evans, P. R.; Murshudov, G. N. How good are my data and what is the resolution? *Acta Crystallogr. D Biol. Crystallogr.* **2013**, *69*, 1204–1214.
- (34) Winn, M. D.; Ballard, C. C.; Cowtan, K. D.; Dodson, E. J.; Emsley, P.; Evans, P. R.; Keegan, R. M.; Krissinel, E. B.; Leslie, A. G. W.; McCoy, A.; McNicholas, S. J.; Murshudov, G. N.; Pannu, N. S.; Potterton, E. A.; Powell, H. R.; Read, R. J.; Vagin, A.; Wilson, K. S. Overview of the CCP4 suite and current developments. *Acta Crystallogr. D Biol. Crystallogr.* **2011**, *67*, 235–242.
- (35) Tickle, I. J.; Flensburg, C.; Keller, P.; Paciorek, W.; Sharff, A.; Vonrhein, C.; Bricogne, G. STARANISO; Global Phasing Ltd.: Cambridge, United Kingdom, 2018.
- (36) McCoy, A. J.; Grosse-Kunstleve, R. W.; Adams, P. D.; Winn, M. D.; Storoni, L. C.; Read, R. J. Phaser crystallographic software. *J. Appl. Crystallogr.* **2007**, *40*, 658–674.
- (37) Emsley, P.; Lohkamp, B.; Scott, W. G.; Cowtan, K. Features and development of Coot. *Acta Crystallogr. D Biol. Crystallogr.* **2010**, *66*, 486–501.
- (38) Kovalevskiy, O.; Nicholls, R. A.; Long, F.; Carlon, A.; Murshudov, G. N. Overview of refinement procedures within REFMAC5: Utilizing data from different sources. *Acta Crystallogr. D Struct. Biol.* **2018**, *74*, 215–227.
- (39) Liebschner, D.; Afonine, P. V.; Baker, M. L.; Bunkóczi, G.; Chen, V. B.; Croll, T. I.; Hintze, B.; Hung, L.-W.; Jain, S.; McCoy, A. J.; Moriarty, N. W.; Oeffner, R. D.; Poon, B. K.; Prisant, M. G.; Read, R. J.; Richardson, J. S.; Richardson, D. C.; Sammito, M. D.; Sobolev,

O. V.; Stockwell, D. H.; Terwilliger, T. C.; Urzhumtsev, A. G.; Videau, L. L.; Williams, C. J.; Adams, P. D. Macromolecular structure determination using X-rays, neutrons and electrons: recent developments in *Phenix*. *Acta Crystallogr. D Struct. Biol.* **2019**, *75*, 861–877.

(40) Berman, H. M.; Westbrook, J.; Feng, Z.; Gilliland, G.; Bhat, T. N.; Weissig, H.; Shindyalov, I. N.; Bourne, P. E. The Protein Data Bank. *Nucleic Acids Res.* **2000**, *28*, 235–242.

(41) Kim, S.-K.; Reddy, S. K.; Nelson, B. C.; Robinson, H.; Reddy, P. T.; Ladner, J. E. A comparative biochemical and structural analysis of the intracellular chorismate mutase (Rv0948c) from *Mycobacterium tuberculosis* H₃₇R_v and the secreted chorismate mutase (y2828) from *Yersinia pestis*. *FEBS J.* **2008**, *275*, 4824–4835.

(42) Berendsen, H. J. C.; van der Spoel, D.; van Drunen, R. GROMACS: A message-passing parallel molecular dynamics implementation. *Comput. Phys. Commun.* **1995**, *91*, 43–56.

(43) Abraham, M. J.; Murtola, T.; Schulz, R.; Páll, S.; Smith, J. C.; Hess, B.; Lindahl, E. GROMACS: High performance molecular simulations through multi-level parallelism from laptops to supercomputers. *SoftwareX* **2015**, *1–2*, 19–25.

(44) Cornell, W. D.; Cieplak, P.; Bayly, C. I.; Gould, I. R.; Merz, K. M., Jr.; Ferguson, D. M.; Spellmeyer, D. C.; Fox, T.; Caldwell, J. W.; Kollman, P. A. A second generation force field for the simulation of proteins, nucleic acids, and organic molecules. *J. Am. Chem. Soc.* **1995**, *117*, 5179–5197.

(45) Case, D. A.; Darden, T. A.; Cheatham, T. E., III; Simmerling, C. L.; Wang, J.; Duke, R. E.; Luo, R.; Walker, R. C.; Zhang, W.; Merz, K. M.; Roberts, B.; Hayik, S.; Roitberg, A.; Seabra, G.; Swails, J.; Götz, A. W.; Kolossváry, I.; Wong, K. F.; Paesani, F.; Vanicek, J.; Wolf, R. M.; Liu, J.; Wu, X.; Brozell, S. R.; Steinbrecher, T.; Gohlke, H.; Cai, Q.; Ye, X.; Wang, J.; Hsieh, M.-J.; Cui, G.; Roe, D. R.; Mathews, D. H.; Seetin, M. G.; Salomon-Ferrer, R.; Sagui, C.; Babin, V.; Luchko, T.; Gusarov, S.; Kovalenko, A.; Kollman, P. A. *AMBER 12*; University of California: San Francisco, 2012.

(46) Jorgensen, W. L.; Madura, J. D. Solvation and conformation of methanol in water. *J. Am. Chem. Soc.* **1983**, *105*, 1407–1413.

(47) Wang, J.; Wolf, R. M.; Caldwell, J. W.; Kollman, P. A.; Case, D. A. Development and testing of a general Amber force field. *J. Comput. Chem.* **2004**, *25*, 1157–1174.

(48) Essmann, U.; Perera, L.; Berkowitz, M. L.; Darden, T.; Lee, H.; Pedersen, L. G. A smooth particle mesh Ewald method. *J. Chem. Phys.* **1995**, *103*, 8577–8593.

(49) Bussi, G.; Donadio, D.; Parrinello, M. Canonical sampling through velocity rescaling. *J. Chem. Phys.* **2007**, *126*, No. 014101.

(50) Parrinello, M.; Rahman, A. Polymorphic transitions in single crystals: A new molecular dynamics method. *J. Appl. Phys.* **1981**, *52*, 7182–7190.

(51) Bartlett, P. A.; Johnson, C. R. An inhibitor of chorismate mutase resembling the transition-state conformation. *J. Am. Chem. Soc.* **1985**, *107*, 7792–7793.

(52) Vamvaca, K.; Vögeli, B.; Kast, P.; Pervushin, K.; Hilvert, D. An enzymatic molten globule: Efficient coupling of folding and catalysis. *Proc. Natl. Acad. Sci. U.S.A.* **2004**, *101*, 12860–12864.

(53) Roderer, K.; Kast, P. Evolutionary cycles for pericyclic reactions – Or why we keep mutating mutases. *CHIMIA* **2009**, *63*, 313–317.

(54) Burschowsky, D.; Thorbjørnsrud, H. V.; Heim, J. B.; Fahrig-Kamarauskaitė, J.; Würth-Roderer, K.; Kast, P.; Krengel, U. Interenzyme allosteric regulation of chorismate mutase in *Corynebacterium glutamicum*: structural basis of feedback activation by Trp. *Biochemistry* **2018**, *57*, 557–573.

Recommended by ACS

Discovery of the Potent and Selective MC4R Antagonist PF-07258669 for the Potential Treatment of Appetite Loss

Michelle R. Garnsey, Matthew F. Sammons, *et al.*

FEBRUARY 19, 2023
JOURNAL OF MEDICINAL CHEMISTRY

READ 

Structural Insights into ATP-Sensitive Potassium Channel Mechanics: A Role of Intrinsically Disordered Regions

Katarzyna Walczewska-Szewc and Wiesław Nowak

FEBRUARY 06, 2023
JOURNAL OF CHEMICAL INFORMATION AND MODELING

READ 

Structural Properties of CXCL4L1 and Its Recognition of the CXCR3 N-Terminus

Ya-Hsin Liu, Shih-Che Sue, *et al.*

JANUARY 10, 2023
BIOCHEMISTRY

READ 

Plasma-Catalytic CO₂ Reforming of Toluene over Hydrotalcite-Derived NiFe/(Mg, Al)_xO_x Catalysts

Lina Liu, Xin Tu, *et al.*

FEBRUARY 17, 2023
JACS AU

READ 

Get More Suggestions >